A Three#Dimensional Study of Wormhole Formation in a Porous Medium: Wormhole Length Scaling and a Rankine Ovoid Model

Water Resources Research

RESEARCH ARTICLE
10.1029/2021WR030627

A Three-Dimensional Study of Wormhole Formation in a Porous Medium: Wormhole Length Scaling and a Rankine Ovoid Model

Wei Li[1], **John T. Germaine**[2], **and Herbert H. Einstein**[1]

[1]Department of Civil and Environmental Engineering, Massachusetts Institute of Technology, Cambridge, MA, USA, [2]Department of Civil and Environmental Engineering, Tufts University, Medford, MA, USA

Key Points:

- Lengths of wormholes resulting from flow and dissolution in a 3-D porous medium follow a power-law distribution
- Wormholes develop by competing for available flow, with many developing initially but a few developing further
- We improve the wormhole length prediction by approximating the 3-D radial flow near the wormhole tip with a Rankine ovoid model

Correspondence to:
W. Li,
weili08@mit.edu

Citation:
Li, W., Germaine, J. T., & Einstein, H. H. (2022). A three-dimensional study of wormhole formation in a porous medium: Wormhole length scaling and a Rankine ovoid model. *Water Resources Research*, *58*, e2021WR030627. https://doi.org/10.1029/2021WR030627

Received 15 JUN 2021
Accepted 27 MAY 2022

Author Contributions:
Conceptualization: Wei Li
Formal analysis: Wei Li
Funding acquisition: Herbert H. Einstein
Investigation: Wei Li
Methodology: Wei Li
Project Administration: Herbert H. Einstein
Supervision: John T. Germaine, Herbert H. Einstein
Visualization: Wei Li
Writing – original draft: Wei Li
Writing – review & editing: John T. Germaine, Herbert H. Einstein

Abstract Understanding how wormholes develop and how they change the permeability of the porous medium is important for many natural and industrial processes in subsurface solid-fluid systems. We conduct core flood tests to study the wormhole formation in a porous medium under different flow rates and at different moments before breakthrough. We show that the wormholes created in core flood tests have lengths following a power-law distribution, with more short ones than long ones. This statistical nature of the wormhole lengths allow one to experimentally study the wormhole competition in 3-D: Many wormholes develop initially near the inlet, but only a few develop further. Our experimental results also show that the existing wormhole-matrix models underestimate wormhole lengths because of the neglected additional pressure drop caused by the radial flow near the wormhole tip. We improve upon the existing models by approximating the radial flow near the wormhole tip with a Rankine ovoid model.

Plain Language Summary Underground fluid flow and chemical reactions often result in wormholes, which are channels that look like tree roots, and significantly increase the permeability of porous rocks. Wormhole formation is relevant in many natural and industrial processes, including the formation of underground caves, CO_2 sequestration and enhanced oil recovery. In this study, wormholes are created in the laboratory by injecting water into porous gypsum cores, and are observed with X-ray CT scanning. We show that the wormhole lengths, like the lengths of many other naturally created patterns (faults, river segments, and fjords), follow a power-law distribution. By comparing the wormholes formed under different flow rates and at different moments, we show that the wormholes develop by competing for available flow. Many wormholes develop initially, but only a few win the competition to develop further. Our experimental results also show that existing models, which simulate the flow in a porous medium with two parts (one with and one without wormholes), underestimate wormhole lengths. We improve upon these models by accounting for the 3-D radial flow near the tip of the wormhole, and accurately predict the wormhole lengths observed in the experiments.

1. Introduction

Wormholes are long finger-like channels that form due to the flow and dissolution heterogeneity in a porous medium. Wormhole formation is common in many natural and industrial processes that involve flow and dissolution, such as gypsum and limestone karst formations (Dreybrodt, 1996; Groves & Howard, 1994; Li & Einstein, 2017; Lipar et al., 2021), melt extraction (Kelemen et al., 1995), geologic CO_2 sequestration (Gouze & Luquot, 2011; Li et al., 2021; Menke et al., 2015; Smith et al., 2013; Wang et al., 2016) and enhanced oil recovery (Fredd & Fogler, 1998; Hoefner & Fogler, 1988). The wormholes provide localized highly permeable paths for the fluid and significantly increase the overall permeability of the porous media, which could lead to favorable- (enhanced oil production) or undesired consequences (sinkholes and leakage of sequestered CO_2). Understanding the collective behavior of wormholes as they develop and accurately predicting their lengths are crucial in the engineering of the aforementioned subsurface systems.

Much of the research on wormhole formations has been focused on the dissolution regimes and breakthrough pore volumes as a result of the flow and reaction conditions (Budek & Szymczak, 2012; Daccord, 1987; Dreybrodt & Gabrovšek, 2019; Fredd & Fogler, 1998; Golfier et al., 2002; Izgec et al., 2010; McDuff et al., 2010; Soulaine et al., 2018; Yoo et al., 2021). Due to the difficulties in monitoring wormholes in 3-D as they form, observations of the wormholes are often made after they break through, and descriptions of their geometries are limited by being qualitative (Li et al., 2019c). The evolution of the number and lengths of wormholes as

Table 1
Experimental Parameters Used in the Core Flood Tests

Symbol	Value	Unit	Variable
L_s	8.5	cm	Gypsum specimen length
D_s	3.5	cm	Gypsum specimen diameter
ρ_r	1.22	g/cm^3	Gypsum density
n	0.48	1	Gypsum porosity
C_{eq}	2.6	g/L	Gypsum solubility in water
k_m	2.5×10^{-10}	cm^2	Gypsum matrix permeability
R_p	1×10^{-4}	cm	Gypsum pore radius based on mercury intrusion
k_r	7.1×10^{-3}	cm/s	Dissolution reaction rate coefficient of gypsum
D	9×10^{-6}	cm^2/s	Diffusivity of calcium ion
Q	$5 \sim 40$	μL/s	Injection flow rates
P_c	400	kPa	Confining stress on the gypsum core
P_b	70	kPa	Back pressure

they form has not been studied in laboratory experiments, although a few numerical and field studies have shown that the wormhole lengths follow a power-law distribution with the exponent around 1 (Cabeza et al., 2020; C. E. Cohen et al., 2008; Lipar et al., 2021; Petrus & Szymczak, 2016; Szymczak & Ladd, 2006, 2009). In addition, many studies rely on models to infer the extension of wormholes in the porous medium (Daccord, Lenormand, & Liétard, 1993; Daccord, Liétard, & Lenormand, 1993; Dong, 2018; Li et al., 2019b; Tardy et al., 2007; Taylor & Nasr-El-Din, 2002). These models assume that the wormholes have such a high permeability that they cause no pressure drop for the flow. Thus the porous medium can be divided into a wormhole section, which spans from the inlet to where the longest wormhole extends, and the rest a matrix section. The lengths of the two sections are predicted based on the measured hydraulic data. We refer to these models as "wormhole-matrix models." Although providing a first-order estimation of the extension of wormholes, the wormhole-matrix models do not specify the diameter of wormholes, nor do they provide experimental justification on whether the lengths of the wormholes are indeed what is predicted.

In this study, we use core flood tests to study the wormhole formation at different moments before they break through. The novelty in our experimental procedure is to end each core flood test when the pressure drop between the inlet and outlet decreases to a fraction of its initial value, then observe the wormhole geometry. This allows us to systematically investigate the development of wormholes and their effect on the permeability of a porous medium. We show that the wormholes created in core flood tests have lengths following a power-law distribution, with more short ones than long ones. The exponent of this power-law distribution (1.4 ± 0.3) is slightly higher than those observed in 2-D numerical studies and field observations. This power-law scaling, with its dependence on the flow stages in the tests, reveals the wormhole competition in 3-D: many wormholes develop initially near the inlet, but only a few develop further. To relate the wormhole lengths to the permeability increase, we first prove that the wormholes observed in the experimental study have high enough permeability to cause negligible pressure drops, then show that the wormhole-matrix model underestimates the wormhole length. We improve upon the wormhole-matrix model by approximating the radial flow near the wormhole tip with a Rankine ovoid model, then accurately predict the wormhole lengths observed in the experiments.

2. Experimental Setup and Methods

2.1. Core Flood Tests

The core flood tests on a gypsum-water system are designed to investigate wormhole formation and its effect on permeability before breakthrough. No. 1 Moulding Plaster manufactured by USG Corporation is used to cast gypsum for its consistency and workability. Distilled water supplied by Portland Spring® is used to flow through the gypsum specimen. Cylindrical gypsum specimens are cast and cut to the size of 3.5 cm in diameter and 8.5 cm in length. The material properties of the laboratory cast gypsum are summarized in Table 1. Gypsum-water systems have been used in many studies on reactive transport processes either as an analog system or as the study object itself (Daccord, 1987).

A computer-controlled triaxial system (see Figure 1a) is used for the core flood tests. The triaxial system controls and monitors the confining stress, axial stress, injection rate, and outlet pressure. It monitors the inlet pressure and axial displacement. Before flowing distilled water, the specimen is saturated overnight in the triaxial system to ensure single-phase flow. The saturation process uses a fully saturated gypsum solution to avoid dissolution.

During each test, a constant flow rate is applied at the specimen inlet with the water injection PVA (pressure-volume-actuator), while a constant pressure is applied at the outlet using the back pressure reservoir. The pressure drop between the inlet and outlet (ΔP_t) decreases as the wormholes develop, and reaches zero at wormhole breakthrough (Figure 1b). The novelty in our experimental procedure is to end each test when ΔP_t decreases to a

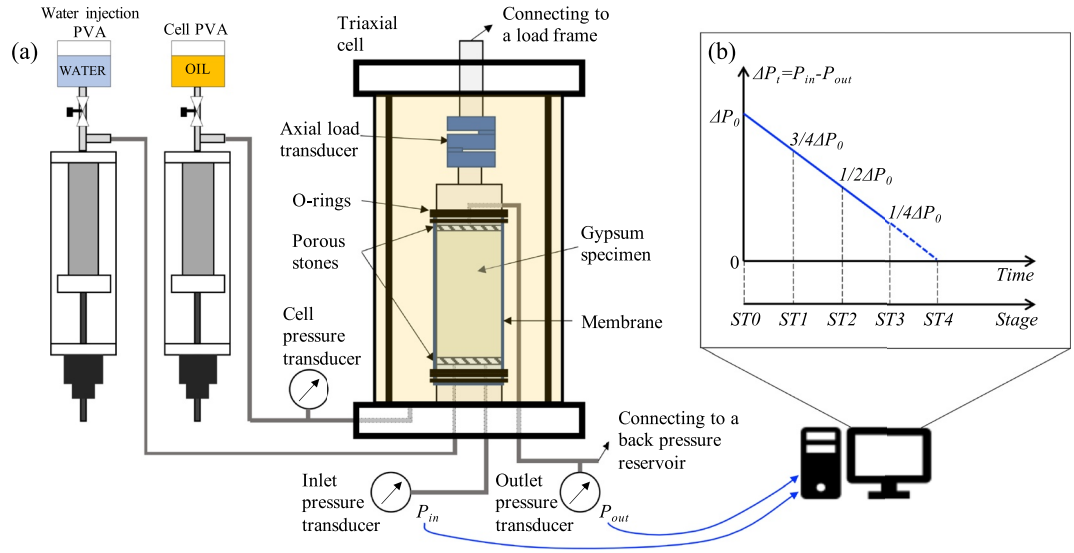

Figure 1. Experimental design for core flood tests. (a) Diagram of the triaxial setup for core flood tests. The inlet- and outlet pressures are monitored by the computer. (b) The pressure drop between the inlet and outlet during core flood tests. As the wormholes form, the pressure drop decreases linearly with time. The pressure drops correspond to the flow stages of the core flood tests.

fraction (P_f) of its initial value (ΔP_0): $P_f = \Delta P_t/\Delta P_0$. This allows us to systematically investigate the development and competition of wormholes before breakthrough. The target values for P_f are 3/4, 1/2, and 1/4, which are referred to as flow stages *ST*1, *ST*2, and *ST*3, respectively (Figure 1b). In this convention, *ST*0 ($\Delta P_t = \Delta P_0$) and *ST*4 ($\Delta P_t = 0$) represent initial state and wormhole breakthrough, respectively.

Previous studies (Fredd & Fogler, 1999; Li et al., 2019a) have shown that it does not require much fluid for the wormholes to break through the specimen (around three pore volumes). Drying and resaturating the specimen involve the displacement of one pore volume of fluid, hence possible sample disturbance. Therefore, each test starts with a new specimen and uses it only once to minimize sample disturbance. The variations between specimens and the resulting wormholes do not allow a one-to-one comparison, so we use the statistics of the wormhole geometry to study the wormhole competition in 3-D.

The core flood test parameters are summarized in Table 1. With these parameters, the following dimensionless quantities are calculated to identify the controlling process among reaction, diffusion and advection in the porous rock matrix (Budek & Szymczak, 2012; Daccord, Lenormand, & Liétard, 1993; Daccord, Liétard, & Lenormand, 1993; Golfier et al., 2002; Li et al., 2019b). The Péclet number (P_e), kinetic parameter (G), and effective Damköhler number (D_{ae}) are defined as:

$$P_e = \frac{2R_c\bar{U}}{D}, \tag{1a}$$

$$G = \frac{2R_c k_r}{DS_h}, \tag{1b}$$

$$D_{ae} = \frac{k_{eff}}{\bar{U}}, \tag{1c}$$

where R_c is the characteristic length of the pores; $\bar{U}$ is the pore-scale average flow velocity $\left(\bar{U} = Q/\left(1/4\pi D_s^2 n\right)\right)$; n is the porosity of gypsum; D is the diffusivity; k_r is the dissolution reaction rate coefficient; S_h is the Sherwood number; k_{eff} is the effective dissolution rate coefficient that accounts for both transport- and reaction-controlled dissolution (Budek & Szymczak, 2012; Li et al., 2019b). The effective dissolution rate coefficient is calculated as:

$$k_{eff} = \frac{k_t k_r}{k_t + k_r}, \tag{2}$$

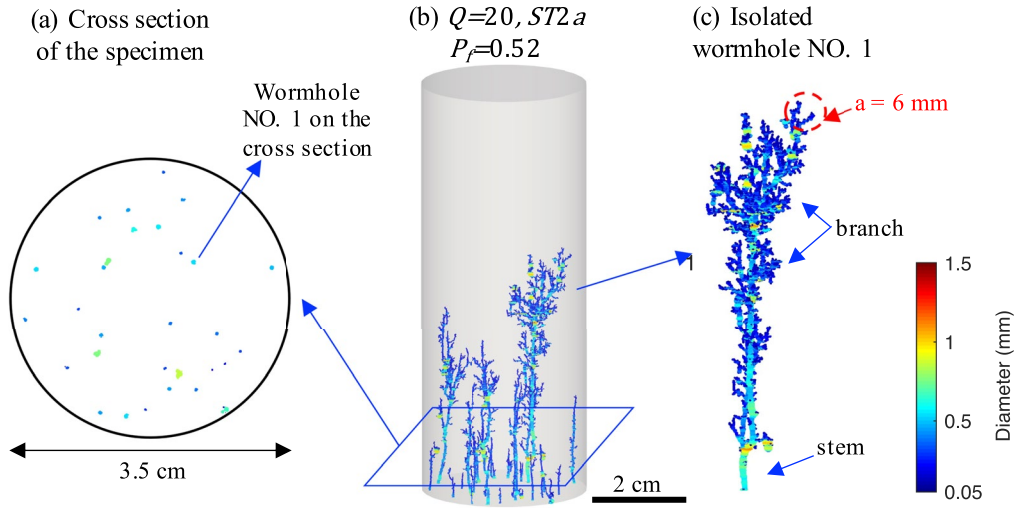

Figure 2. Algorithm to process 3-D wormhole data. (a) A cross section of the specimen. The interceptions between this cross section and the wormholes are shown as circular patches. The areas of these patches are used to calculate the equivalent diameters of the branches and stems. (b) Experimental results of test with $Q = 20$ μL/s, *ST2a* as an example. (c) Isolated biggest wormhole. Each wormhole is defined as one connected 3-D volume. The stem and branch are defined similar to those of a river. The tip of the biggest wormhole has multiple branches that distribute the flow, which makes a source radius (a) of around 6 mm (see Section 3.3.2 for details).

where k_r is the dissolution reaction rate coefficient; and k_t is the transport-controlled dissolution rate coefficient and is calculated as: $k_t = \frac{S_h D}{2R_c}$.

The Péclet number (P_e) quantifies the rate of advection relative to that of diffusion. The pore radius (R_p) measured using mercury intrusion porosimetry (Li et al., 2019a) or the square root of permeability (Daccord, Lenormand, & Liétard, 1993) can be used as the characteristic length (R_c) for the porous matrix. The estimated Péclet number is in the order of 10^{-3}, indicating that advection is much slower than diffusion in the pore space. The kinetic parameter (G) compares the rates of reaction and diffusion during dissolution. With an approximated value $S_h = 4$ for the Sherwood number in a porous medium (Budek & Szymczak, 2012), the kinetic parameter is in the order of 10^{-2}, indicating that the dissolution is reaction-controlled. The effective Damköhler number compares the rate of dissolution to that of advection. The effective Damköhler number ranges from 0.76 to 6.09, corresponding to the flow rate of 40 to 5 μL/s in the core flood tests. The Damköhler numbers indicate comparable rates for advection and reaction, while Li et al. (2019b) argue that the major pore flow has higher velocity due to flow heterogeneity, hence advection has higher rate than reaction.

Therefore, the relative rates of the three processes are: reaction < advection < diffusion. Based on these dimensionless quantities, the dissolution regime is "ramified wormholes" with more wormholes under lower Damköhler number (higher flow rates) (Budek & Szymczak, 2012; Golfier et al., 2002; Li et al., 2019b), as verified by the experimental results (Figure 3).

2.2. CT Scanning and Analysis

After the core flood tests, the specimens are dried in a 40°C oven and CT scanned. The specimens are scanned at a 50-micron voxel resolution, which resolves the detailed geometry of the wormholes (~mm), but not the pore networks in the rock matrix (~100 nm according to Li et al. (2019a)). The CT scanner outputs the scanning result as image stack of horizontal cross sections of the specimen. Since the specimen material is almost pure gypsum, the image is easily converted to a binary matrix, with ones representing the void (initial pores and wormholes) voxels and zeros representing the gypsum matrix voxels. These binary images are stacked to form an initial 3-D binary matrix to represent the 3-D specimen. In this 3-D binary matrix, each connected component of ones represents either a pore or a wormhole (Figure 2c). The pores, with their diameters around 300 μm, are the result of trapped air bubbles during casting (Li et al., 2019a). A 1000-voxel 3-D filter and a 2.5 mm length filter are used to

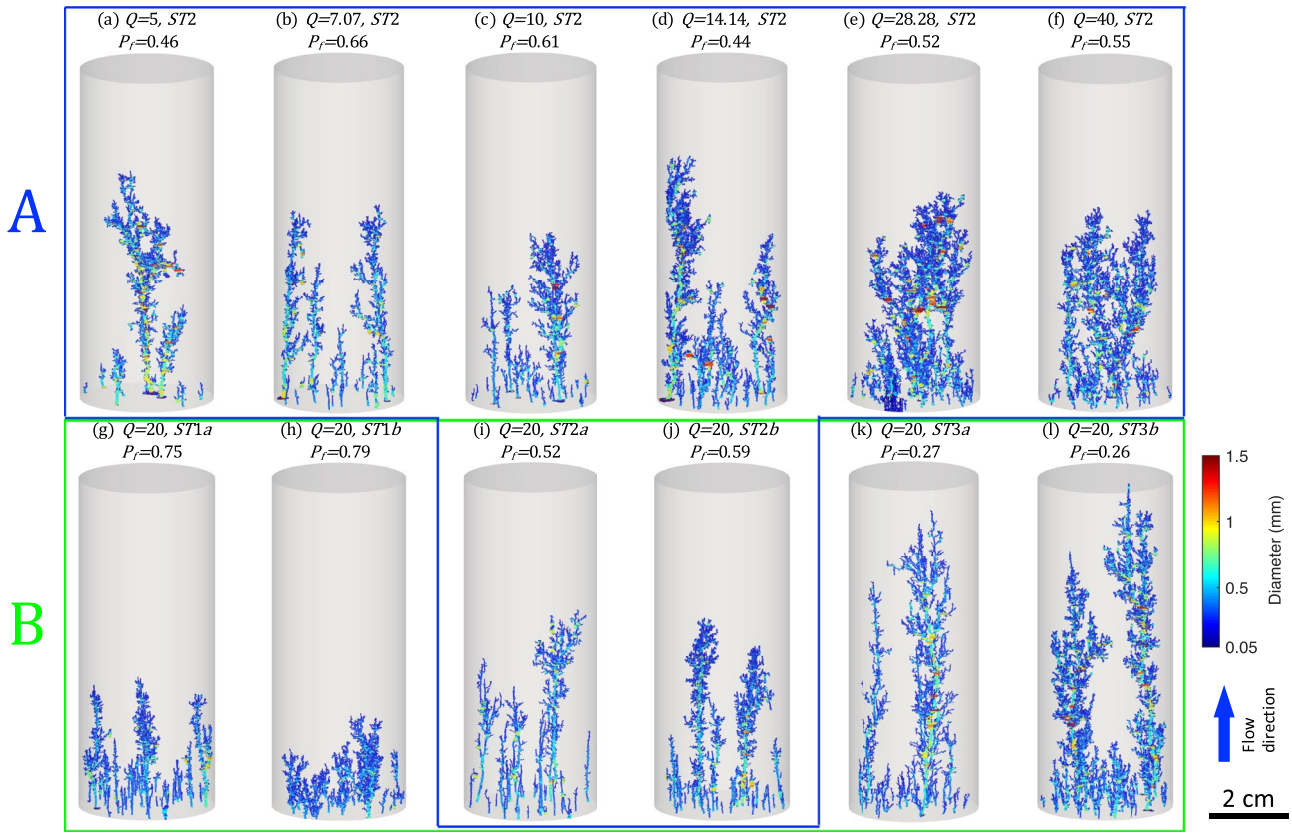

Figure 3. Wormholes resulting from the 12 core flood tests. The flow rate (Q, μL/s), the target flow stage (ST), and the actual fraction of pressure drop (P_f) are indicated on top of each specimen. The wormholes are color coded by the equivalent diameter of each stem and branch, with warmer colors representing larger diameters and cooler colors representing smaller diameters. The tests are designed this way so that the effect of flow rates and flow stages on wormhole formation can be studied with Group A and Group B, respectively. The wormholes shown in panels (i and j) are used in the studies with both groups.

remove the pores and wormholes shorter than 2.5 mm. Each of the resulting wormholes has a stem and branches similar to the stem and branches of a river (Figure 2c). We refer to the stem and branches as conduits in general in the following discussion.

To calculate the diameter of each conduit of the wormhole, the horizontal cross section of the 3-D binary matrix is analyzed as shown in Figure 2a. The circular patches on each cross section plane represent the intersection between the conduits and this plane. Each patch on this plane has N_{ai} voxels, which represent the area $A_{ct} = N_{vi} \times 50 \times 50\ \mu m^2$. Since the wormhole conduits are mostly vertical, their intersection with the horizontal cross section are approximately their cross sections. This allows one to calculate the equivalent diameter of the conduits D_e on each plane:

$$D_e = \sqrt{4A_{ct}/\pi}. \tag{3}$$

An additional filter is applied on each horizontal cross section to remove circular patches that have D_e smaller than 0.1 mm. The resulting 3-D binary matrix then represents wormholes that have conduit diameters larger than 0.1 mm and lengths longer than 2.5 mm. With this clear definition of sizes, this final 3-D binary matrix is used for wormhole reconstruction (Figure 2b) and isolated wormhole geometry analysis (Figure 2c). The wormholes are color coded by the equivalent diameter of each conduit, with warmer colors indicating larger diameters. For instance, the diameter of the stem with a cyan color is larger than those of the branches with a blue color in Figure 2c.

3. Results

3.1. 3-D Wormhole Reconstruction

The wormholes resulting from the 12 core flood tests and the parameters of each test are summarized in Figure 3. The flow rate (Q in μL/s) and the target flow stage (ST) are used as identifiers for the tests. The actual fraction of pressure drop (P_f) when the test was ended is also indicated on top of each specimen. In the core flood test, the distilled water is injected at the bottom of the specimen, as indicated in Figure 3. The wormholes are color coded the same way as in Figure 2c. The wormholes resulting from tests under different flow rates but ended at the same flow stage ($ST2$) are grouped as Group A. The wormholes resulting from tests under $Q = 20$ μL/s but ended at different flow stages are grouped as Group B. The tests are designed this way so that the effect of the Damköhler number (flow rate) and flow stage on wormhole formation can be studied with Group A and Group B, respectively.

In the 12 tests, the reconstructed wormholes in 3-D all initiate from the inlet of the specimen and extend partially into the specimen, as shown in Figure 3. The wormholes have a tapered geometry with a larger diameter near the inlet than the rest, as indicated by the warmer colors. The tests ended at $ST2$ result in wormholes that extend roughly to the middle of the specimen, as shown by the Group A wormholes. The tests ended at later flow stages (e.g., $ST3$) result in longer wormholes, as shown by the Group B wormholes.

3.2. Wormhole Lengths

3.2.1. Scaling Behavior of Wormhole Lengths

To quantitatively analyze the geometry of the wormholes, each wormhole is isolated to measure its extension into the specimen. Figure 4a shows the individual wormholes from Figure 3i ordered by their volumes, from the biggest to the smallest. There are in total 28 wormholes resulting from the test with $Q = 20.00$ μL/s, $ST2a$, most of which are short. Because of the tilting and tortuous nature of the wormholes, the length of a wormhole is hard to quantify. Therefore, the vertical extension of the wormhole from the inlet of the specimen to the wormhole tip is defined as the wormhole length in the following discussion. The wormhole lengths (L_w) are then normalized by the specimen diameter (D_s) to study their scaling properties. The normalized wormhole lengths for each core flood test are summarized in Figures 4b and 4c for Groups A and B, respectively. The cumulative distribution (N_{wh}) of the number of normalized wormhole lengths greater than a particular value of L_{wh}/D_s are plotted. For each test, this number N_{wh} is normalized by the total number of wormholes in this test (N_{whT}) for the plot. After this normalization, the distribution of all tests start from $\ln(N_{wh}/N_{whT}) = 0$. Since all the wormholes are longer than 2.5 mm, the data points plateau when $\ln(L_{wh}/D_s) < \ln(2.5/35) = -2.64$.

Beyond this plateau, the wormhole lengths follow a power-law distribution (Figures 4b and 4c), with more short wormholes than long ones. A linear fit of the data points beyond the plateau ($\ln(L_{wh}/D_s) = -2.64$) in the log-log plot is used to quantify this power-law distribution:

$$\frac{N_{wh}}{N_{whT}} \sim \left(\frac{L_{wh}}{D_s}\right)^{-m}. \tag{4}$$

The exponent m of each test is included in the legends of Figures 4b and 4c and summarized for the two groups of tests in Figures 4d and 4e, with the same markers as in the plots above. The power-law distribution of the wormhole lengths has an exponent m of 1.4 ± 0.3. The power-law distribution of wormhole lengths shows its scale-invariant property: scaling the wormhole length by a factor only result in a proportionally scaled power-law distribution of the lengths. Similar power-law scaling has been observed in the lengths of 2-D patterns, such as viscous fingers and dissolution channels in a fracture (Budek et al., 2015; Cabeza et al., 2020; C. E. Cohen et al., 2008; Roy et al., 1999; Szymczak & Ladd, 2006, 2009), with their exponents m around 1. In our study, the wormholes, forming in a 3-D porous medium, have lengths following a power-law distribution with the exponent m around 1.4, which is slightly higher than the exponents reported for the 2-D patterns (Budek & Szymczak, 2012; Cabeza et al., 2020; C. E. Cohen et al., 2008; Szymczak & Ladd, 2006). This indicates that there are proportionally more short wormholes in a 3-D system than in a 2-D system. For this experimental study, however, the length scale is limited to the diameter of the specimen D_s. If a longer specimen is used and the wormholes are allowed to develop further beyond D_s, it is unlikely that the same power-law scaling will continue.

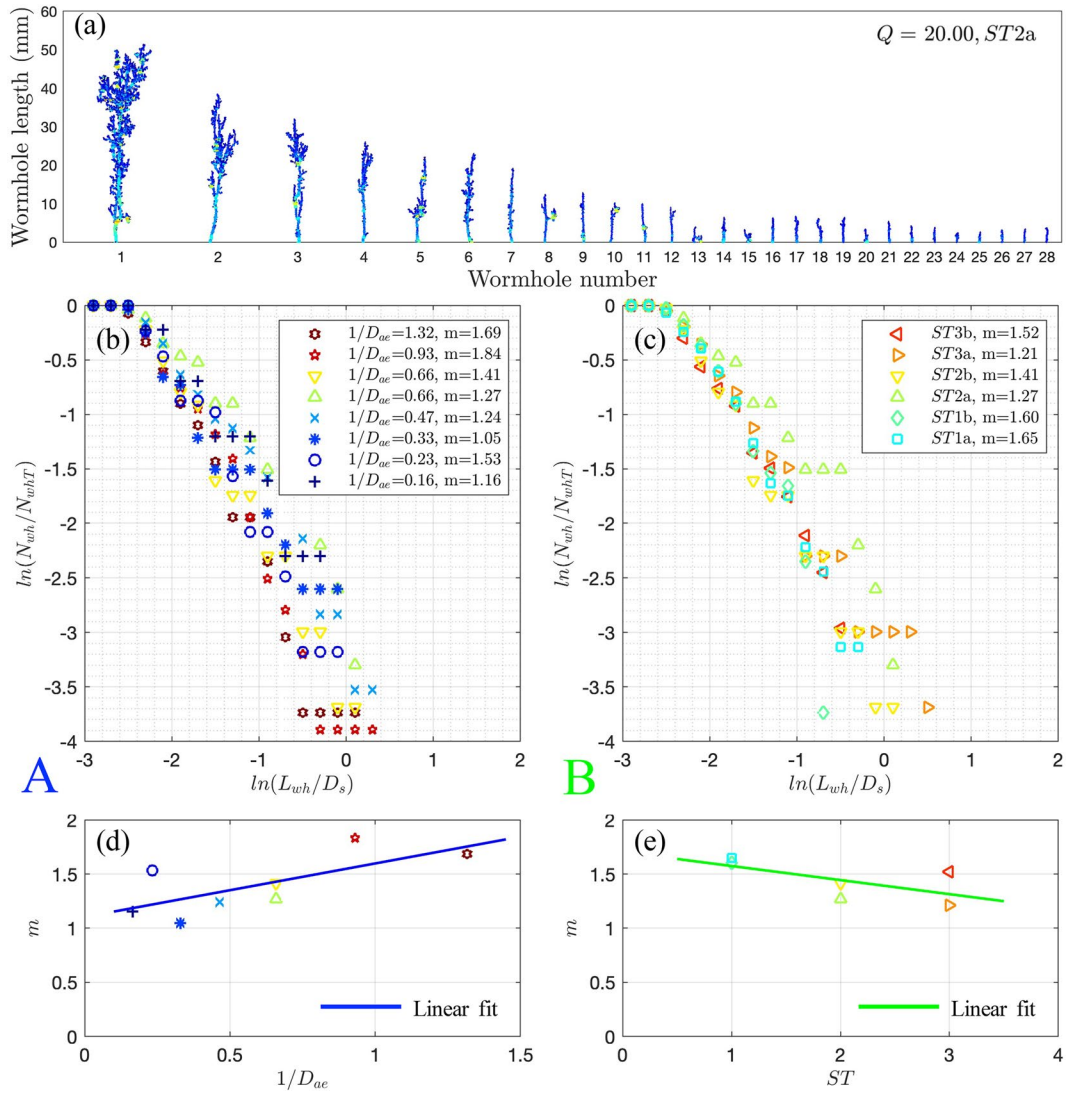

Figure 4. Quantitative analysis of wormhole length. (a) Individual wormholes from Figure 3i ordered by their volumes. (b) The lengths of wormholes in the Group A tests follow a power-law distribution. All the tests are ended at *ST*2, with higher inverse Damköhler number ($1/D_{ae}$) corresponding to higher flow rates and steeper power-law distribution. (c) The lengths of wormholes in the Group B tests follow a power-law distribution. All the tests have the inverse Damköhler number of 0.66, but are ended at different stages. Tests ended at later stages corresponds to more gradual power-law distribution. (d) Exponent *m* of the power-law distribution of the wormhole lengths for the Groups A tests. The tests with higher inverse Damköhler number correspond to steeper power-law distribution. (e) Exponent *m* of the power-law distribution of the wormhole lengths for the Groups B tests. The tests ended at later stages correspond to more gradual power-law distribution. The markers are the same as in the plots above.

3.2.2. 3-D Wormhole Competition

During the core flood tests, dissolution causes permeability to increase locally, which enhances the flow of reactants and promotes further dissolution. Having larger diameters (the critical value is derived in Appendix A) than the pores, the wormholes provide localized highly permeable paths for the flow and reactant. Among the wormholes, the longer ones, having a shorter distance to the outlet and thus causing a higher pressure gradient in the adjacent porous matrix, are likely to conduct more flow and develop faster. Collectively, we see wormholes develop by competing for flow (Cabeza et al., 2020; Hoefner & Fogler, 1988; Szymczak & Ladd, 2006).

The exponent *m*, as a function of flow rates and flow stages, can be used to study the wormholes competition in 3-D. For wormholes resulting from tests under different flow rates but ended at the same stage (Group A), the

exponent m is summarized in Figure 4d. The inverse Damköhler number is used as the X-axis, which is proportional to the flow rate according to Equation 1c and Fredd and Fogler (1998) and Li et al. (2019b). The exponent m has a positive trend indicating that the lengths of wormholes resulting from higher inverse Damköhler numbers (higher flow rates) follow a steeper power-law distribution. This steeper distribution shows that although higher inverse Damköhler numbers (higher flow rates) result in more wormholes, most of which are short. In other words, the wormholes resulting from higher inverse Damköhler numbers (higher flow rates) have a higher portion of short wormholes than the wormholes resulting from higher Damköhler numbers (lower flow rates).

For tests with the same Damköhler numbers but ended at different flow stages (Group B, Figures 4c and 4e), the exponent m has a negative trend showing that the wormhole lengths at the later flow stages follow a more gradual power-law distribution than those at the early stages. The scale-invariant property of wormhole length does not continue when the wormholes develop in the later stages beyond the scale of the system D_s. Instead, they develop disproportionally with the few longer ones developing further and short ones ceasing to develop.

By studying the power-law scaling of the wormhole lengths, we show that the 3-D wormholes develop through competition. The wormholes compete for flow to induce dissolution and further extension into the porous medium. Initially, many wormholes develop from the inlet due to the availability of flow at the inlet. As the dissolution continues, the longer wormholes create preferred avenues for the flow to the outlet and convey more flow locally. In contrast, the short ones having less available flow then cease to develop.

3.3. Wormhole-Induced Permeability Change

The statistical analysis of the wormhole lengths shows how the wormholes compete to develop under different flow rates and at different flow stages. We then use these findings to study the effect of wormholes on the overall permeability of the specimen. To do so, a critical wormhole diameter is first estimated to identify the diameter of wormholes that significantly increases the permeability of the porous medium and causes negligible pressure drop. We found that the experimentally observed wormholes (Figure 3) all cause negligible pressure drop. This is consistent with the assumptions of a wormhole-matrix model, which, however, does not accurately predict the evolution of specimen permeability as a function of the wormhole lengths. We then improve upon the wormhole-matrix model by using a Rankine ovoid model to approximate the radial flow near the wormhole tip.

3.3.1. Estimation of the Critical Wormhole Diameter

From a microscopic perspective, wormholes are part of the pore network in a porous medium except for their much greater diameters and higher permeability than the pores. Therefore, a discussion of wormhole lengths should always be related to the definition of their diameters. The discussion in the previous section is based on wormholes with diameters larger than 0.1 mm. In this section, we first evaluate the assumption of the wormhole-matrix model that the wormholes cause negligible pressure drop, by estimating the diameter of conduits that significantly increase the permeability. We use a cubic representative elementary volume (REV, see Figure A1) of size L_{rev} to estimate the diameter of wormholes that contribute greatly to the permeability of the porous medium. The derivation (see Appendix A) shows that the diameters of the wormholes (D_{cw}) to increase the permeability to N_p times that of the intact rock matrix is:

$$D_{cw} = \left(\frac{128}{\pi} \cdot N_p \cdot k_m \cdot \frac{L_{rev}^2}{N_{cd}} \right)^{\frac{1}{4}}, \tag{5}$$

where k_m is the permeability of the intact rock matrix; N_{cd} is the number of conduits intersecting the REV cross section with an area of L_{rev}^2. Here, we refer to D_{cw} as the critical wormhole diameter. D_{cw} is an estimation of the wormhole diameter when the permeability of the REV is significantly increased. It is not a cut-off diameter to distinguish the wormholes from the rest of the pores in the pore network. Although the choice for the multiplier N_p is subjective, the estimation will not differ much for either $N_p = 10$ or $N_p = 100$ because of the 1/4 power on N_p.

To obtain the parameter $\frac{L_{rev}^2}{N_{cd}}$, we plot the number of conduits (N_{cd}) and the total area of these conduits normalized by the cross-section area (S_{ch}) on each cross section of each specimen (Figure 5). The results of each specimen

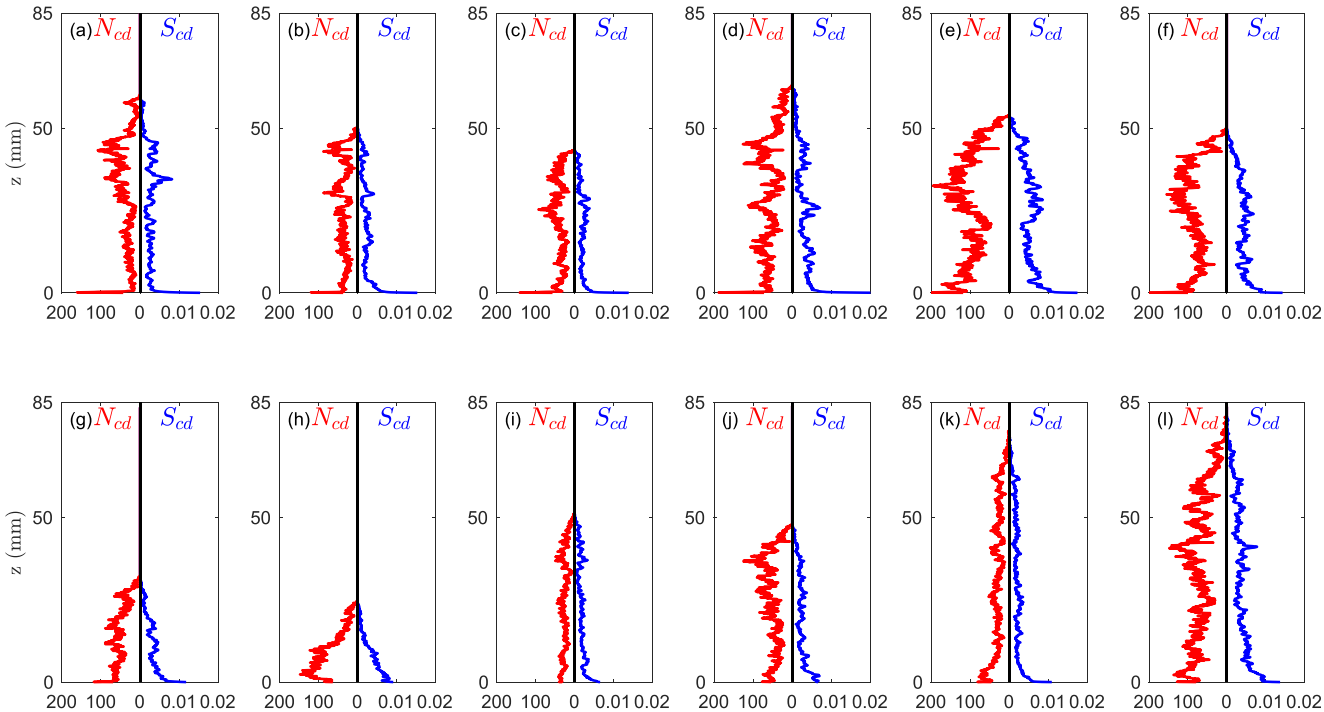

Figure 5. Number of conduits (N_{cd}) and normalized total conduit area (S_{ch}) on each horizontal cross section of each specimen.

are arranged in the same order as the reconstructions shown in Figure 3. On each cross section, the number of intersecting conduits are in the order of 100, while the total area of these conduits are less than 0.1% of the cross-section area. Therefore the parameter $\frac{L_{rev}^2}{N_{cd}}$ is around 0.1 cm^2.

Based on the experimental parameters listed in Table 1, D_{cw} can be estimated for the core flood tests. Assuming the wormholes significantly increased the permeability, say 10 times as high as that of the rock matrix, the critical diameter of the wormhole calculated based on Equation 5 is around 0.1 mm. This is the same as the minimum diameter of wormholes reconstructed in Figure 3. This calculation shows that the experimentally observed wormholes in Figure 3 are the ones that significantly increase the permeability of the specimen and cause negligible pressure drop during the flow tests. This is consistent with the assumptions of the wormhole-matrix model, which is then used to predict the wormhole lengths based on the specimen permeability and compared with the experimental results.

3.3.2. Relation Between Wormhole Lengths and Specimen Permeability

The core flood tests produce the wormhole lengths and the hydraulic data at the moment when the wormholes stopped developing. These data can be used to relate the wormhole lengths to the overall specimen permeability (k_s). According to the Darcy's law, k_s in the core flood tests can be calculated as:

$$k_s(t) = \frac{4\mu Q}{\pi D_s^2} \frac{L_s}{\Delta P_t}, \tag{6}$$

where μ is the dynamic viscosity of the pore fluid; Q is the flow rate; D_s is the specimen diameter; L_s is the specimen length; and ΔP_t is the pressure drop at time t. Before wormhole formation, the overall permeability of the specimen equals to the permeability of the porous matrix: $k_s|_{t=0} = k_m$. Assuming a constant fluid dynamic viscosity μ during the core flood test, the evolution of the overall permeability of the specimen can be directly related to the evolution of the pressure drop:

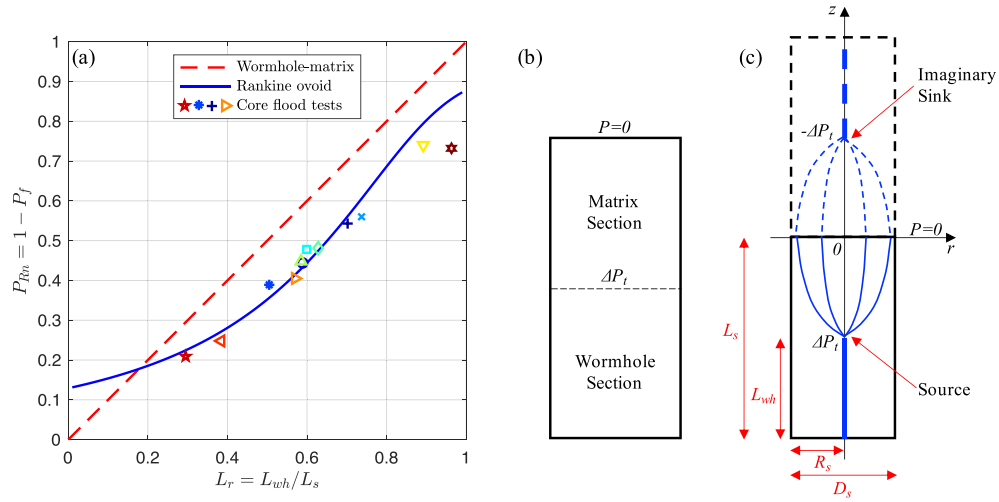

Figure 6. Relation between wormhole length and permeability. (a) Relative wormhole length and normalized reduction of pressure drop. The markers of the 12 test data points are the same as those in Figure 4a. (b) Schematic of a wormhole-matrix model. The wormhole section, having the same length as the longest wormhole, causes no pressure drop. The pressure drop at time t (ΔP_t) is acting only on the matrix section. (c) Rankine ovoid model accounting for the radial flow near the tip of the wormhole. The solid black rectangle represents a porous rock core with the longest wormhole (solid blue line). The dashed lines represent their imaginary part mirrored to the plane $z = 0$. The tips of the wormholes are the source and sink of the Rankine ovoid.

$$k_s(t) = \frac{\Delta P_0}{\Delta P_t} k_m = \frac{1}{P_f} k_m, \tag{7}$$

where P_f is the fraction of pressure drop as defined in Section 2.1. In the following discussion, we use the pressure drop as the variable to study the relation between wormhole lengths and specimen permeability.

Figure 6b is a schematic of the wormhole-matrix model for linear flow core flood tests. The wormhole-matrix model assumes that the wormholes cause negligible pressure drop in the core flood tests. This is verified by the analysis in the previous section. Therefore, the measured pressure drop (ΔP_t) is then only caused by the matrix section. As the wormhole section extends under constant flow rate, the length of the matrix section decreases, so does the pressure drop (ΔP_t).

The mathematical description for the wormhole-matrix model can be written by nondimensionalize wormhole section length and reduction of pressure drop. We define the normalized reduction of pressure drop (P_{Rn}) as:

$$P_{Rn} = \frac{\Delta P_0 - \Delta P_t}{\Delta P_0}, \tag{8}$$

where ΔP_0 is the initial pressure drop between the inlet and outlet; and ΔP_t is the pressure drop at time t. Given the definition of the fraction of pressure drop $P_f = \Delta P_t / \Delta P_0$, P_{Rn} can also be expressed as: $P_{Rn} = 1 - P_f$. We define the relative wormhole section length (L_r) as the ratio of the longest wormhole length to the specimen length: $L_r = \max(L_{wh})/L_s$. According to the wormhole-matrix model, the two dimensionless quantities have the relation:

$$P_{Rn} = L_r. \tag{9}$$

Equation 9 describes the wormhole-matrix model for a linear flow with a constant flow rate, where the reduction of pressure drop and increase of permeability are caused by the extension of the wormhole section. Despite its simplicity, this model has been used to estimate the length of the longest wormholes, which is often invisible in laboratory and field studies.

The L_r and P_{Rn} of the 12 core flood tests are compared with the predictions of the wormhole-matrix model in Figure 6a. The experimental results all fall below the line $P_{Rn} = L_r$, indicating that the wormholes extended

further than what the wormhole-matrix model predicts. For example, in the tests ended at $ST2$ ($P_{Rn} \sim 0.5$, the relative wormhole lengths are around 0.6 (Figure 6a)), which are about 20% longer than the prediction made by the wormhole-matrix model.

This discrepancy indicates that there is an additional pressure drop that the wormhole-matrix model does not consider. This additional pressure drop is caused by the radial flow from the wormhole tip to the porous matrix, as discussed in several 2-D numerical studies (Cabeza et al., 2020; Cheung & Rajaram, 2002; Dreybrodt & Gabrovšek, 2019; Petrus & Szymczak, 2016). To study the radial flow in 3-D, we developed a Rankine ovoid model (White, 2011) to approximate the flow field as shown in Figure 6c. This Rankine ovoid consists of a background pressure gradient $\left(-\frac{\Delta P_t}{L_s}\right)$, a source (wormhole tip) and a sink (imaginary). With this approximation, the relation between P_{Rn} and L_r can be expressed as:

$$\begin{aligned} P_{Rn} &= 1 - \frac{\Delta P_t}{\Delta P_0} \\ &= 1 - \frac{1}{1 + \frac{4aL_s}{R_s^2} \cdot \left(1 - \frac{L_s(1 - L_r)}{\sqrt{L_s^2(1 - L_r)^2 + R_s^2}}\right)}. \end{aligned} \tag{10}$$

where a is the radius of the source; and R_s is the radius of the cylindrical specimen. The modeling development and derivation can be found in Appendix B. The relation between P_{Rn} and L_r predicted by the Rankine ovoid model is shown in Figure 6a and compared with the predictions by the wormhole-matrix model and the experimental data. The experimental parameters such as the specimen radius ($R_s = 35$ mm) and length ($L_s = 85$ mm) of the specimen are used in the Rankine ovoid model. Since the wormhole tip has multiple branches that extend out to help distribute the flow (Figures 2c and 3), the source radius $a = 6$ mm is chosen to account for the effect of these branches in the Rankine ovoid model. The Rankine ovoid model predicts a pressure curve that falls mostly below the line $P_{Rn} = L_s$ and agrees with the test results. The Rankine ovoid model shows that the radial flow near the wormhole tip indeed causes an additional pressure drop. By accounting for the pressure drop caused by the 3-D radial flow near the wormhole tip, the Rankine ovoid model provides a more accurate prediction of the wormhole length than the wormhole-matrix model.

Admittedly, the Rankine ovoid model is an approximation of the complex geometry of wormholes, their interactions with the porous matrix and the resulting complex flow field. Discrepancies arise at the very initial state of wormhole formation when the source is the inlet surface of the specimen instead of the tip of the dominant wormhole. At this initial state, the assumption of radial flow is no longer accurate for the flow condition. Mismatch also occurs right before wormhole breakthrough when the wormholes are so close to the outlet that there is no place to develop the radial flow and that the limited permeability of the one or two conduit at the tip causes pressure drop. To capture the higher resolution detail of the flow field caused by the complex wormholes, numerical models would be more appropriate.

Nevertheless, by considering the 3-D radial flow near the wormhole tip, the Rankine ovoid model improves upon the existing wormhole-matrix model to provide a better approximation of the flow condition. The Rankine ovoid model can be applied to field studies where the detailed geometries of the wormholes are not observable. In this case, the radial flow near the wormhole tip could cause larger pressure drops because of the larger size of the porous matrix to flow into, according to the Rankine ovoid model. Using the hydraulic data with the Rankine ovoid model avoids the underestimation of wormhole lengths and the unexpected early occurrence of the wormhole breakthrough. This is particularly useful when estimating the extension of karst formations, solution pipes and the penetration distance of acid stimulation.

4. Discussion

Power-law distributions have been used in many empirical laws, such as Gutenberg-Richter law for earthquakes and Hack's law for river basins, to describe the statistic feature of natural processes. The power law also encompasses many pattern formations in geoscience, such as faults (Clark et al., 1999), fjords (Bak, 1996), solution

pipes (Corral & González, 2019; Lipar et al., 2021; Petrus & Szymczak, 2016), and river networks (Dodds & Rothman, 2000). The power-law scaling of the pattern formations in reality has upper and lower bounds, for example, a fjord cannot be smaller than a water molecule or bigger than a tectonic plate (Bak, 1996). Nevertheless, there is a great range of length scales that the power law covers. The power-law scaling can be used to predict the size and lengths of the pattern formations in geoscience.

In the context of this study, the centimeter-scale wormhole lengths follow a power-law distribution, as do the meter-scale lengths of sinkholes or solution pipes, which the wormholes later become (Lipar et al., 2021). This shows the potential of using the power law to unify the laboratory observations with field observations. This unified power law could greatly contribute to the effort of evaluating the risks of karst formation hazard (Bodenner, 2018; Brinkmann, 2013), the integrity of CO_2 reservoir caprock (Smith et al., 2013), and the efficiency of acid stimulation (Fredd & Fogler, 1998).

However, challenges for this effort are to obtain reliable data of the wormhole and sinkhole, since the resolutions and sensitivities of the observation techniques used for different scales are often not comparable. Field studies have coarser resolution and lower sensitivity than laboratory studies. On the other hand, laboratory studies are limited by the specimen size and aspect ratio, which affect the observable size and number of wormholes and can potentially skew the power-law distribution (C. E. Cohen et al., 2008). These issues with the data could be the cause for the different exponents observed in field studies ($m \sim 1$) and our laboratory study ($m = 1.4 \pm 0.3$).

5. Conclusions

We conduct core flood tests to study the wormhole formation in a porous medium under different flow rates and at different moments before breakthrough. The novelty in our experimental procedure is to end each test based on the reduction of pressure drop so that we can observe the 3-D wormhole evolution before breakthrough. We showed that the wormhole lengths in each specimen follow a power-law distribution, with the exponent being a function of the flow rate and flow stage. The exponent m for power-law scaling of wormhole lengths is 1.4 ± 0.3, which is slightly higher than the exponents reported for the 2-D patterns (viscous fingers and dissolution channels). We use these statistics of wormhole lengths to show how wormholes develop by competing for flow. Many wormholes develop from the inlet due to the initial availability of flow at the inlet. As the competition continues, the longer wormholes create preferred avenues for the flow to the outlet and convey more flow locally, while the shorter ones having less available flow then cease to develop. While the concept of wormholes developing by competing for available flow has been used in numerical studies (Cabeza et al., 2020; Szymczak & Ladd, 2006; Wang et al., 2016), our study provides experimental justification for this concept in a 3-D porous medium before the breakthrough.

We also estimate the critical wormhole diameter that significantly increases the permeability of the porous medium and show that it is within the same order of magnitude as those of the wormholes observed in our experiments. This is consistent with the assumption of the wormhole-matrix model that the wormholes cause no pressure drop. Yet, our wormhole length data and pressure data show that the existing wormhole-matrix models underestimate the extension of wormholes. To improve upon these models, we use a Rankine ovoid model to approximate the 3-D flow in the specimen, specifically the additional pressure drop caused by the radial flow near the wormhole tip. By accounting for this radial flow, our improved model accurately captures the relation between wormhole lengths and permeability. This will be particularly useful when using hydraulic data to estimate the extension of karst formations, solution pipes and the penetration distance of acid stimulation.

The experimental study is conducted with careful definition of wormhole diameters and lengths. The power-law scaling of the wormhole lengths can potentially unify the laboratory observations with field observations on sinkhole depth. This unified power law could greatly contribute to the effort of evaluating the risks of karst formation hazard, the integrity of CO_2 reservoir caprock, and the efficiency of acid stimulation.

Appendix A: Derivation for the Critical Wormhole Diameter

A cubic REV of size L_{rev} (Figure A1) is used to represent a part of the specimen with N_{cd} tubular conduits forming the preferred flow paths with a larger size (D_w) than the rest of the pore network(not shown). L_{rev} here is in the scale of centimeters so that both the conduits and rock matrix can fit in the REV. Due to the positive feedback between the flow and dissolution, these conduits will enlarge much more than the rest of the pore network. To simplify the discussion, we assume all the conduits in the REV have the same diameter (D_w) that increases due to dissolution.

We use k_{rev}, k_w and k_m to represent the homogenized permeabilities of the REV, the wormholes and the matrix, respectively. According to Darcy's law, the flow rate in the REV can be expressed as:

$$Q_{rev} = L_{rev}^2 \frac{k_{rev}}{\mu} \cdot \left(\frac{\Delta P_{rev}}{L_{rev}} \right), \tag{A1}$$

where μ is the dynamic viscosity of the pore fluid; ΔP_{rev} is the pressure drop across the REV. The flow in the REV consists of the flow in the wormholes (Q_w) and the matrix (Q_m), thus Equation A1 can be expressed as:

$$Q_{rev} = Q_w + Q_m = L_{rev}^2 \frac{k_m}{\mu} \cdot \left(\frac{\Delta P_{rev}}{L_{rev}} \right) + L_{rev}^2 \frac{k_w}{\mu} \cdot \left(\frac{\Delta P_{rev}}{L_{rev}} \right). \tag{A2}$$

Therefore, the homogenized permeability of the REV (k_{rev}) can be expressed as $k_{rev} = k_w + k_m$. The homogenized permeability of the wormholes k_w represents the contribution of wormholes to the permeability of the REV, instead of the permeability of a specific wormhole. It is determined by the diameter of the wormholes (D_w), as well as the number of conduits (N_{cd}) in the REV. Assume the flow in the wormholes is laminar pipe flow, the total flow in the N_{cd} conduits Q_w can be expressed as:

$$Q_w = N_{cd} \cdot \frac{\pi D_w^4}{128\mu} \cdot \left(\frac{\Delta P_{rev}}{L_{rev}} \right); \tag{A3}$$

where μ is the dynamic viscosity of the fluid; $\frac{\Delta P_{rev}}{L_{rev}}$ is the pressure gradient along the flow direction in the REV. Thus the permeability contributed by the conduits can be calculated by the Darcy's law:

$$k_w = \frac{\mu \cdot Q_w}{L_{rev}^2} \cdot \left(\frac{L_{rev}}{\Delta P_{rev}} \right) = \frac{N_{cd}}{L_{rev}^2} \cdot \frac{\pi D_w^4}{128}. \tag{A4}$$

When the conduits significantly increase the permeability to N_p times as high as that of the intact rock matrix ($k_w = N_p \cdot k_m$), the diameters of the wormholes (D_{cw}) can be calculated by replacing k_w with $N_p \cdot k_m$ in Equation A4. This diameter is referred to as the critical wormhole diameter:

$$D_{cw} = \left(\frac{128}{\pi} \cdot N_p \cdot k_m \cdot \frac{L_{rev}^2}{N_{cd}} \right)^{\frac{1}{4}}. \tag{A5}$$

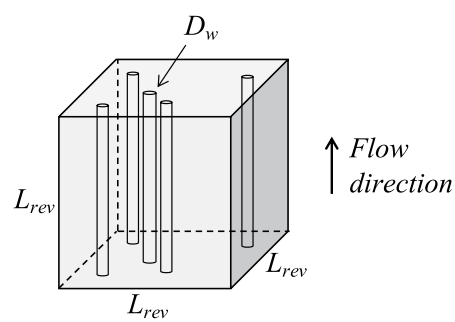

Figure A1. Schematic of a representative elementary volume of the porous medium with conduits.

Appendix B: Derivation for the Rankine Ovoid Model

The flow from the wormholes to the porous rock matrix can be simplified to a 3-D axisymmetric flow in the cylindrical $(r-z)$ coordinates in Figure 6c. Since the evolution of the wormhole geometry is much slower than that of the flow, we can use quasi-static approximation, in which the flow and dissolution are at steady state for a particular wormhole geometry. The boundary conditions are, constant pressure ΔP_t at the inlet ($z=-L_s$) and along the wormhole ($r=0$, $-L_s<z<(L_s-L_{wh})$); constant pressure ($P=0$) at the outlet ($z=0$); and no flow boundary condition at the cylindrical specimen sidewall ($r=R$, $-L_s<z<0$). For 3-D flow in a porous medium, analytical solutions exist for a line source with constant flux (White, 2011), and a parabolic source with constant pressure (Nilson & Griffiths, 1990). For 2-D flow in a porous medium, Y. Cohen et al. (2015) derived the analytical solution for a line source with constant pressure using conformal mapping. To the authors' best knowledge, there is no analytical solution that accounts for both the background pressure gradient and uniform pressure singularity along a wormhole in 3-D. It is not in the scope of this study to develop such analytical solution. Instead, we use the Rankine ovoid model to approximate the flow field in the specimen and study the additional pressure drop caused by the radial flow.

Because of the background pressure gradient $(-\Delta P_t/L_s)$ and the constant pressure (ΔP_t) along the wormhole, most of the flow occurs at the tip of the wormhole. This indicates that a Rankine ovoid model can be used to approximate the flow near the wormhole tip. As shown in Figure 6c, at time t when the wormhole extends to L_{wh} long, the pressure drop is ΔP_t. The background pressure gradient is $-\Delta P_t/L_s$, of which the negative sign indicates the pressure decreases along the z-axis. The tip of the wormhole is the source with the pressure ΔP_t, while an imaginary sink ($-\Delta P_t$, dashed blue line) is at the mirror position to the line $z=0$. The source-sink pair and the background pressure gradient forms a Rankine ovoid, of which the steady-state pressure can be expressed as:

$$P(z,r)=\Delta P_t\cdot\frac{a}{\sqrt{(L_1+z)^2+r^2}}-\Delta P_t\cdot\frac{a}{\sqrt{(L_1-z)^2+r^2}}+\left(-\frac{\Delta P_t}{L_s}\right)z. \tag{B1}$$

where a is the radius of the source and sink; and L_1 is the distance from the source to the origin, $L_1=L_s-L_{wh}$. The vertical flux u_z at $z=0$ is:

$$u_z|_{z=0}=-\frac{k}{\mu}\cdot\frac{\partial P}{\partial z}|_{z=0}=\frac{2ka}{\mu}\cdot\frac{\Delta P_t L_1}{\left(L_1^2+r^2\right)^{\frac{3}{2}}}+\frac{k}{\mu}\cdot\frac{\Delta P_t}{L_s}. \tag{B2}$$

We delineate the geometry of the specimen in this infinite flow field as shown in Figure 6c. This is an approximation of the flow field in the specimen, where, unlike the infinite flow field, the vertical boundaries are impermeable. By integrating the flux across the outlet area of the specimen, the flow rate Q can be expressed as:

$$\begin{aligned}Q|_{z=0}&=\int_0^{R_s}u_z|_{z=0}2\pi r dr\\&=\frac{4\pi ka}{\mu}\cdot\Delta P_t\left(1-\frac{L_1}{\sqrt{L_1^2+R_s^2}}\right)+\frac{\pi R_s^2 k}{\mu}\cdot\frac{\Delta P_t}{L_s}.\end{aligned} \tag{B3}$$

Assume the initial pressure, P_0 is the pressure when there is no wormhole:

$$Q=\frac{\pi R_s^2 k}{\mu}\cdot\frac{\Delta P_0}{L_s} \tag{B4}$$

Since the core flood tests use constant flow rate, the flow rates expressed in Equations B3 and B4 are equal, which yields:

$$\frac{\Delta P_t}{\Delta P_0}=\frac{1}{1+\frac{4aL_s}{R_s^2}\cdot\left(1-\frac{L_1}{\sqrt{L_1^2+R_s^2}}\right)}. \tag{B5}$$

Given the relation between L_1 and L_r: $L_1=L_s(1-L_r)$, P_{Rn} can then be expressed as a function L_r:

$$P_{Rn} = 1 - \frac{\Delta P_t}{\Delta P_0} = 1 - \frac{1}{1 + \frac{4aL_s}{R_s^2} \cdot \left(1 - \frac{L_s(1 - L_r)}{\sqrt{L_s^2(1 - L_r)^2 + R_s^2}}\right)}. \quad \text{(B6)}$$

Data Availability Statement

The experimental data supporting this work are publicly available online (https://doi.org/10.17632/wzc6cc2z4z.2).

Acknowledgments
This work was funded by the Abu Dhabi National Oil Company.

References

Bak, P. (1996). *How nature works: The science of self-organized criticality*. Springer.
Bodenner, C. (2018). *The science behind Florida's sinkhole epidemic*. Smithsonian Magazine. Retrieved from https://www.smithsonianmag.com/science-nature/science-behind-floridas-sinkhole-epidemic-180969158/
Brinkmann, R. (2013). *Florida sinkholes: Science and policy*. University Press of Florida.
Budek, A., Garstecki, P., Samborski, A., & Szymczak, P. (2015). Thin-finger growth and droplet pinch-off in miscible and immiscible displacements in a periodic network of microfluidic channels. *Physics of Fluids*, *27*(11), 112109. https://doi.org/10.1063/1.4935225
Budek, A., & Szymczak, P. (2012). Network models of dissolution of porous media. *Physical Review E*, *86*(5), 056318. https://doi.org/10.1103/physreve.86.056318
Cabeza, Y., Hidalgo, J. J., & Carrera, J. (2020). Competition is the underlying mechanism controlling viscous fingering and wormhole growth. *Geophysical Research Letters*, *47*(3), e2019GL084795. https://doi.org/10.1029/2019gl084795
Cheung, W., & Rajaram, H. (2002). Dissolution finger growth in variable aperture fractures: Role of the tip-region flow field. *Geophysical Research Letters*, *29*(22), 32-1–32-4. https://doi.org/10.1029/2002gl015196
Clark, R. M., Cox, S., & Laslett, G. M. (1999). Generalizations of power-law distributions applicable to sampled fault-trace lengths: Model choice, parameter estimation and caveats. *Geophysical Journal International*, *136*(2), 357–372. https://doi.org/10.1046/j.1365-246x.1999.00728.x
Cohen, C. E., Ding, D., Quintard, M., & Bazin, B. (2008). From pore scale to wellbore scale: Impact of geometry on wormhole growth in carbonate acidization. *Chemical Engineering Science*, *63*(12), 3088–3099. https://doi.org/10.1016/j.ces.2008.03.021
Cohen, Y., Devauchelle, O., Seybold, H. F., Robert, S. Y., Szymczak, P., & Rothman, D. H. (2015). Path selection in the growth of rivers. *Proceedings of the National Academy of Sciences*, *112*(46), 14132–14137. https://doi.org/10.1073/pnas.1413883112
Corral, A., & González, A. (2019). Power law size distributions in geoscience revisited. *Earth and Space Science*, *6*(5), 673–697. https://doi.org/10.1029/2018ea000479
Daccord, G. (1987). Chemical dissolution of a porous medium by a reactive fluid. *Physical Review Letters*, *58*(5), 479–482. https://doi.org/10.1103/physrevlett.58.479
Daccord, G., Lenormand, R., & Liétard, O. (1993). Chemical dissolution of a porous medium by a reactive fluid—I. Model for the "wormholing" phenomenon. *Chemical Engineering Science*, *48*(1), 169–178. https://doi.org/10.1016/0009-2509(93)80293-y
Daccord, G., Liétard, O., & Lenormand, R. (1993). Chemical dissolution of a porous medium by a reactive fluid—II. Convection vs reaction, behavior diagram. *Chemical Engineering Science*, *48*(1), 179–186. https://doi.org/10.1016/0009-2509(93)80294-z
Dodds, P. S., & Rothman, D. H. (2000). Geometry of river networks. I. Scaling, fluctuations, and deviations. *Physical Review E*, *63*(1), 016115. https://doi.org/10.1103/physreve.63.016115
Dong, K. (2018). A new wormhole propagation model at optimal conditions for carbonate acidizing. *Journal of Petroleum Science and Engineering*, *171*, 1309–1317. https://doi.org/10.1016/j.petrol.2018.08.055
Dreybrodt, W. (1996). Principles of early development of karst conduits under natural and man-made conditions revealed by mathematical analysis of numerical models. *Water Resources Research*, *32*(9), 2923–2935. https://doi.org/10.1029/96wr01332
Dreybrodt, W., & Gabrovšek, F. (2019). Dynamics of wormhole formation in fractured limestones. *Hydrology and Earth System Sciences*, *23*(4), 1995–2014. https://doi.org/10.5194/hess-23-1995-2019
Fredd, C. N., & Fogler, H. S. (1998). Influence of transport and reaction on wormhole formation in porous media. *AIChE Journal*, *44*(9), 1933–1949. https://doi.org/10.1002/aic.690440902
Fredd, C. N., & Fogler, H. S. (1999). Optimum conditions for wormhole formation in carbonate porous media: Influence of transport and reaction. *SPE Journal*, *4*(3), 196–205. https://doi.org/10.2118/56995-pa
Golfier, F., Zarcone, C., Bazin, B., Lenormand, R., Lasseux, D., & Quintard, M. (2002). On the ability of a Darcy-scale model to capture wormhole formation during the dissolution of a porous medium. *Journal of Fluid Mechanics*, *457*, 213–254. https://doi.org/10.1017/s0022112002007735
Gouze, P., & Luquot, L. (2011). X-ray microtomography characterization of porosity, permeability and reactive surface changes during dissolution. *Journal of Contaminant Hydrology*, *120*, 45–55. https://doi.org/10.1016/j.jconhyd.2010.07.004
Groves, C. G., & Howard, A. D. (1994). Early development of karst systems: 1. Preferential flow path enlargement under laminar flow. *Water Resources Research*, *30*(10), 2837–2846. https://doi.org/10.1029/94wr01303
Hoefner, M., & Fogler, H. S. (1988). Pore evolution and channel formation during flow and reaction in porous media. *AIChE Journal*, *34*(1), 45–54. https://doi.org/10.1002/aic.690340107
Izgec, O., Zhu, D., & Hill, A. D. (2010). Numerical and experimental investigation of acid wormholing during acidization of vuggy carbonate rocks. *Journal of Petroleum Science and Engineering*, *74*(1–2), 51–66. https://doi.org/10.1016/j.petrol.2010.08.006
Kelemen, P. B., Whitehead, J., Aharonov, E., & Jordahl, K. A. (1995). Experiments on flow focusing in soluble porous media, with applications to melt extraction from the mantle. *Journal of Geophysical Research*, *100*(B1), 475–496. https://doi.org/10.1029/94jb02544
Li, W., & Einstein, H. H. (2017). Theoretical and numerical investigation of the cavity evolution in gypsum rock. *Water Resources Research*, *53*(11), 9988–10001. https://doi.org/10.1002/2017wr021776

Li, W., Einstein, H. H., & Germaine, J. T. (2019a). An experimental study of matrix dissolution and wormhole formation using gypsum core flood tests: 1. Permeability evolution and wormhole geometry analysis. *Journal of Geophysical Research: Solid Earth*, *124*(11), 11055–11073. https://doi.org/10.1029/2018jb017238

Li, W., Einstein, H. H., & Germaine, J. T. (2019b). An experimental study of matrix dissolution and wormhole formation using gypsum core flood tests: 2. Dissolution kinetics and modeling. *Journal of Geophysical Research: Solid Earth*, *124*(11), 11074–11088. https://doi.org/10.1029/2019jb018092

Li, W., Einstein, H. H., & Germaine, J. T. (2019c). Geometric and fractal analysis of complex wormholes resulting from gypsum core flood tests. In *53rd US Rock Mechanics/Geomechanics Symposium*.

Li, W., Germaine, J. T., & Einstein, H. H. (2021). Transport-controlled dissolution in an evolving fracture: The extended Purday solution and fracture flow tests. *Water Resources Research*, *57*(3), e2020WR029166. https://doi.org/10.1029/2020wr029166

Lipar, M., Szymczak, P., White, S. Q., & Webb, J. A. (2021). Solution pipes and focused vertical water flow: Geomorphology and modelling. *Earth-Science Reviews*, *218*, 103635. https://doi.org/10.1016/j.earscirev.2021.103635

McDuff, D., Shuchart, C. E., Jackson, S., Postl, D., Brown, & James, S. (2010). Understanding wormholes in carbonates: Unprecedented experimental scale and 3-D visualization. In *SPE Annual Technical Conference and Exhibition*.

Menke, H. P., Bijeljic, B., Andrew, M. G., & Blunt, M. J. (2015). Dynamic three-dimensional pore-scale imaging of reaction in a carbonate at reservoir conditions. *Environmental Science & Technology*, *49*(7), 4407–4414. https://doi.org/10.1021/es505789f

Nilson, R. H., & Griffiths, S. K. (1990). Wormhole growth in soluble porous materials. *Physical Review Letters*, *65*(13), 1583–1586. https://doi.org/10.1103/physrevlett.65.1583

Petrus, K., & Szymczak, P. (2016). Influence of layering on the formation and growth of solution pipes. *Frontiers in Physics*, *3*, 92. https://doi.org/10.3389/fphy.2015.00092

Roy, A., Roy, S., Bhattacharyya, A., Banerjee, S., & Tarafdar, S. (1999). Discrete scale invariance in viscous fingering patterns. *The European Physical Journal B-Condensed Matter and Complex Systems*, *12*(1), 1–3. https://doi.org/10.1007/s100510050966

Smith, M. M., Sholokhova, Y., Hao, Y., & Carroll, S. A. (2013). CO_2-induced dissolution of low permeability carbonates. Part I: Characterization and experiments. *Advances in Water Resources*, *62*, 370–387. https://doi.org/10.1016/j.advwatres.2013.09.008

Soulaine, C., Roman, S., Kovscek, A., & Tchelepi, H. A. (2018). Pore-scale modelling of multiphase reactive flow: Application to mineral dissolution with production of CO_2. *Journal of Fluid Mechanics*, *855*, 616–645. https://doi.org/10.1017/jfm.2018.655

Szymczak, P., & Ladd, A. (2006). A network model of channel competition in fracture dissolution. *Geophysical Research Letters*, *33*(5), L05401. https://doi.org/10.1029/2005gl025334

Szymczak, P., & Ladd, A. (2009). Comment on: "From pore scale to wellbore scale: Impact of geometry on wormhole growth in carbonate acidization by CE Cohen et al. [Chemical Engineering Science 63, 3088–3099, 2008]". *Chemical Engineering Science*, *64*(12), 3029–3030. https://doi.org/10.1016/j.ces.2009.02.048

Tardy, P. M. J., Lecerf, B., & Christanti, Y. (2007). An experimentally validated wormhole model for self-diverting and conventional acids in carbonate rocks under radial flow conditions. In *European Formation Damage Conference*.

Taylor, K., & Nasr-El-Din, H. (2002). Coreflood evaluation of in-situ gelled acids. In *International Symposium and Exhibition on Formation Damage Control*.

Wang, H., Bernabé, Y., Mok, U., & Evans, B. (2016). Localized reactive flow in carbonate rocks: Core-flood experiments and network simulations. *Journal of Geophysical Research: Solid Earth*, *121*(11), 7965–7983. https://doi.org/10.1002/2016jb013304

White, F. M. (2011). *Fluid mechanics*. McGraw Hill.

Yoo, H., Kim, Y., Jang, H., & Lee, J. (2021). Propagation characteristics of optimum wormhole in carbonate matrix acidizing using micro X-ray CT imaging. *Journal of Petroleum Science and Engineering*, *196*, 108010. https://doi.org/10.1016/j.petrol.2020.108010